

The individual abundance distributions of disc stars across birth radii in GALAH

Kaile Wang¹,^{*} Andreia Carrillo²,^{*} Melissa K. Ness^{3,4} and Tobias Buck⁵

¹Department of Astronomy, University of Texas at Austin, 2515 Speedway, Stop C1400, Austin, TX 78712-1205, USA

²Institute for Computational Cosmology, Department of Physics, Durham University, Durham DH1 3LE, UK

³Department of Astronomy, Columbia University, Pupin Physics Laboratories, New York, NY 10027, USA

⁴Center for Computational Astrophysics, Flatiron Institute, 162 5th Avenue, New York, NY 10010, USA

⁵Leibniz-Institut für Astrophysik Potsdam (AIP), An der Sternwarte 16, D-14482 Potsdam, Germany

Accepted 2023 October 12. Received 2023 October 10; in original form 2023 June 1

ABSTRACT

Individual abundances in the Milky Way disc record stellar birth properties [e.g. age, birth radius (R_{birth})], and capture the diversity of the star-forming environments over time. Assuming an analytical relationship between ($[\text{Fe}/\text{H}]$, $[\alpha/\text{Fe}]$), and R_{birth} , we examine the distributions of individual abundances $[\text{X}/\text{Fe}]$ of elements C, O, Mg, Si, Ca (α), Al (odd- z), Mn (iron-peak), Y, and Ba (neutron-capture) for stars in the Milky Way. We want to understand how these elements might differentiate environments across the disc. We assign tracks of R_{birth} in the $[\alpha/\text{Fe}]$ versus $[\text{Fe}/\text{H}]$ plane as informed by expectations from simulations for $\sim 59\,000$ GALAH stars in the solar neighborhood ($R \sim 7\text{--}9$ kpc) which also have inferred ages. Our formalism for R_{birth} shows that older stars (~ 10 Gyrs) have an R_{birth} distribution with smaller mean values (i.e. $\bar{R}_{\text{birth}} \sim 5 \pm 0.8$ kpc) compared to younger stars (~ 6 Gyrs; $\bar{R}_{\text{birth}} \sim 10 \pm 1.5$ kpc), for a given $[\text{Fe}/\text{H}]$, consistent with inside-out growth. The α -, odd- z , and iron-peak element abundances decrease as a function of R_{birth} , whereas the neutron-capture abundances increase. The $R_{\text{birth}}\text{--}[\text{Fe}/\text{H}]$ gradient we measure is steeper compared to the present-day gradient (-0.066 dex kpc $^{-1}$ versus -0.058 dex kpc $^{-1}$), which we also find true for $R_{\text{birth}}\text{--}[\text{X}/\text{Fe}]$ gradients. These results (i) showcase the feasibility of relating the birth radius of stars to their element abundances, (ii) demonstrate that the Milky Way abundance gradients across R_{birth} have evolved to be shallower over time, and (iii) offer an observational comparison to element abundance distributions in hydrodynamical simulations.

Key words: Galaxy: abundances – Galaxy: disc – Galaxy: evolution.

1 INTRODUCTION

Recovering the birth conditions of the stars is one of the main goals of Galactic archaeology. However, stars deviate from their birth orbits, such that their guiding-centre radius can change over their lifetime, without leaving any signature of this change. These orbital excursions are due to processes such as the interaction with the spiral structure as well as external perturbations from infalling satellites (e.g. Sellwood & Binney 2002; Minchev & Quillen 2006; Quillen et al. 2009; Minchev et al. 2012). Although we cannot directly probe the initial orbital properties of disc stars at birth, they exhibit atmospheric abundances that – to first order – reflect the abundance distribution of the gas from which the stars were born, with exceptions (e.g. Iben 1965; Bahcall & Loeb 1990; Dotter et al. 2017; Shetrone et al. 2019).

We can therefore assume that most element abundances of stars, in particular within narrow regions of evolutionary state, are time-invariant. With stellar death, elements created within the stars and during explosive nucleosynthesis are returned to the interstellar medium. This enriches the environment where newer stars are

formed, in a cyclic process. The element abundances for a given star are therefore a record of the nucleosynthetic history of the star-forming environment, at that particular time and place. The time invariance of element abundances and their effective barcode of a star’s birth environment has been foundational to the idea of chemical tagging, via which individual molecular cloud stellar birth sites in the disc might be reconstructed using abundances alone (Freeman & Bland-Hawthorn 2002). However, the current data appear to demonstrate that this goal is prohibited by the low-dimensionality of what appears to be a very correlated abundance space (Ting, Conroy & Goodman 2015; Kos et al. 2018; Ness et al. 2019; Griffith et al. 2021; de Mijolla et al. 2021; Ness et al. 2022; Weinberg et al. 2022). A more feasible goal with current spectroscopic data is the inference of the time and overall radius at which stars formed in the disc.

Different types of stars and production mechanisms produce elements across the periodic table with different yields, at different rates, and at different points in time (see Kobayashi, Karakas & Lugaro 2020). Additionally, it is widely accepted that galaxies, like the Milky Way, formed inside-out, with star formation starting in the deepest part of the potential and proceeding outwards (e.g. González Delgado et al. 2015; Frankel et al. 2019). Combining nucleosynthesis time-scales with the inside-out formation of the Milky Way, the

* E-mail: kailewang@utexas.edu

element abundances of the stars encode the temporal enrichment of the Galaxy and reveal stars' birth properties in terms of age and spacial location. We are now able to have a clearer picture of this as the field of Galactic archaeology has greatly expanded due to large multi-object stellar surveys, such as the Apache Point Observatory Galactic Evolution Experiment (APOGEE; Majewski et al. 2017; Abdurro'uf et al. 2022), the Galactic Archaeology with HERMES (GALAH; Buder et al. 2021), *Gaia*-European Southern Observatory (ESO) survey (*Gaia*-ESO; Gilmore et al. 2012), *Gaia* Radial Velocity Spectrometer survey (*Gaia*; Recio-Blanco et al. 2023), and the Large Sky Area Multi-Object Fibre Spectroscopic Telescope (Cui et al. 2012; Zhao et al. 2012). These surveys enable the detailed study of the element abundance for $>10^5$ stars in the Galaxy.

In addition to element abundances, another fundamental and time-invariant property of stars is their age. Age tells us *when* during the evolution of the Galaxy a star was formed. In fact, numerous studies have explored the relationship between stellar age and element abundances, or age-[X/Fe] relations (Hayden et al. 2022; Carrillo et al. 2023; Ratcliffe & Ness 2023). These studies have shown that just by knowing a star's age and metallicity, [Fe/H], the element abundance, [X/Fe], can be predicted up to a precision of 0.02 dex for many elements. Indeed, a star's age does prove to be a key link to understanding the nucleosynthetic history and evolution of the Galaxy. The only missing link now is *where* in the Galaxy a star was born. If we know a star's individual abundances, age, and birth site, we can begin to unravel the formation of the Milky Way disc with utmost detail.

To this effect, the element abundances of stars should be yet very useful. Earlier works have demonstrated the feasibility to infer birth radius, R_{birth} . For example, Minchev et al. (2018) presented a largely model-independent approach for estimating R_{birth} for Milky Way disc stars, using [Fe/H] and age estimates from the local HARPS sample (Adibekyan et al. 2012). The assumptions relied on are (1) the interstellar medium (ISM) is well mixed at a given radius, (2) there exists a negative radial metallicity gradient in the ISM for most of the disc lifetime, (3) stars younger than 1 Gyr are expected to have little migration, and (4) the Milky Way formed inside-out. Utilizing the R_{birth} derived in their work, they find that the ISM radial metallicity gradient in the Milky Way disc flattens with time. As noted in this study, processes like radial migration can blur R_{birth} signatures. With this in mind, Frankel et al. (2018) developed a model to derive R_{birth} by quantifying the radial migration in the Milky Way disc, using the ages and [Fe/H] of low- α disc stars. In this work, it was assumed that (i) the metallicity of the ISM has negligible variations azimuthally, (ii) the Milky Way had a relatively quiescent life for the past 8 Gyr, and (iii) radial orbit migration is the only mechanism responsible for the scatter in age-metallicity at a given radius. Their model reproduced the observed data well and further found that the radial orbit migration efficiency in the Milky Way is strong. Recently, Lu et al. (2022a) proposed an empirical method to derive birth radii from age and metallicity measurements, with the assumptions that gas is well mixed in Galactic azimuth, Milky Way formed inside-out, and there is a well-defined linear relation between metallicity and birth radius. Such in-depth studies to derive R_{birth} have been shown to be successful, with the help of various physically motivated assumptions and modelling. It is therefore worth asking if R_{birth} could be similarly derived with different assumptions, and specifically a model that does not directly use present-day radius measurements. In addition, as detailed element abundances have been shown to have a direct link to ages, it is interesting to explore how detailed element abundances can potentially trace stars back to their birth sites.

Fortunately, the correlations between the birth radius and stellar properties have also been shown from cosmological hydrodynamical simulations, allowing methods of recovering the birth radius of stars to be explored. For example, Lu et al. (2022b) examined the reliability of inferring birth radii from the assumed linear relationship between the ISM metallicity with radius, using four zoom-in cosmological hydrodynamic simulations from the Numerical Investigation of a Hundred Astronomical Objects-Ultra High Definition (NIHAO-UHD) project (Buck 2020; Buck et al. 2020). They found that precise stellar birth radii can be obtained for stars with age <10 Gyr, as the stellar disc starts to form and the linear correlation between the ISM metallicity and radius increases. Also with the simulations from the NIHAO-UHD project, Buck (2020) showed the direct correlation between element abundances (specifically, [O/Fe] and [Fe/H]) and the birth location of stars. Similar birth radius trends have also been seen in other cosmological simulations. For example, Clarke et al. (2019) showed how α -bimodality could arise due to clumpy star formation, and they similarly noted the distribution of stars with different birth radii on the [Fe/H]-[O/Fe] plane.

In this work, we want to recover the birth radius of stars simply based on their $[\alpha/\text{Fe}]$ and [Fe/H] abundances, as shown in simulation works (e.g. Buck 2020). Instead of performing complex Galactic chemical evolution modelling, we assign each of the stars a birth radius based on their $[\alpha/\text{Fe}]$ and [Fe/H] abundances and examine the validity of this birth radius assignment. To do this, we explore the individual abundance distribution [X/Fe] across birth radii with the disc stars in GALAH DR3 data (Buder et al. 2021). In Section 2, we describe the observational data we used in this study. In Section 3, we discuss our birth radius assignment and the simulation work we are motivated by. In Section 4, we present our age-birth radius relation in two thin metallicity bins, and in Section 5, we show the distribution of individual element abundances [X/Fe] across birth radii. The results presented in these two sections validate our birth radius assignment based on element abundances. Lastly, we summarize and discuss the results in Section 6.

2 OBSERVATIONAL DATA

We take advantage of the GALAH survey data release 3 (DR3; Buder et al. 2021) which measures up to 30 element abundance ratios for elements in different groups: α , light/odd-z, iron-peak, and neutron-capture. The GALAH survey uses the HERMES instrument, a high-resolution ($R \sim 28\,000$) four channel fibre-fed spectrograph (covering 4713–4903, 5648–5873, 6478–6737, and 7585–7887 Å) on the Anglo-Australian Telescope (De Silva et al. 2015). The catalogue contains 588 571 stars, with the stellar parameters determined using the modified version of the spectrum synthesis code Spectroscopy Made Easy (Valenti & Piskunov 1996; Piskunov & Valenti 2017) and 1D MARCS (Model Atmospheres with a Radiative and Convective Scheme) model atmospheres. After the stellar parameters were estimated and fixed, one abundance was fitted at a time for the different lines/elements in the GALAH wavelength range (Buder et al. 2021). In this work, we aim to study the distribution of individual abundances [X/Fe], which we take to be $X = \alpha, \text{C}, \text{O}, \text{Mg}, \text{Al}, \text{Si}, \text{Ca}, \text{Mn}, \text{Y}, \text{and Ba}$, spanning the different groups of elements.

In addition to the main catalogue, we also use the GALAH DR3 value-added catalogue that contains stellar ages, Galactic kinematics, and dynamics. The stellar ages were determined by the Bayesian Stellar Parameter Estimation code, an isochrone-based scheme that provides a Bayesian estimate of intrinsic stellar parameters from observed parameters by making use of stellar isochrones, adopting a flat prior on age and metallicity (Sharma et al. 2018). The Galactic

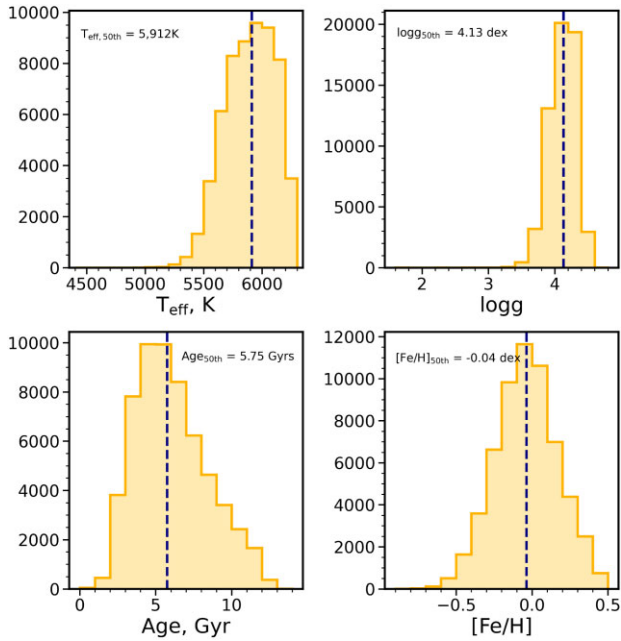


Figure 1. Distribution of stellar parameters (effective temperature T_{eff} , surface gravity $\log g$, stellar age, and metallicity $[\text{Fe}/\text{H}]$) for the parent sample of 59 237 qualified disc stars. The vertical dashed lines mark the median of the distributions.

dynamic information was calculated using `galpy` (Bovy 2015). In the calculations, the best-fitting axisymmetric potential by McMillan (2017) was used with a solar radius of 8.21 kpc.

We assemble a parent sample of qualified GALAH DR3 disc stars according to the following criteria:

- (i) $\text{flag_sp}=0$, $\text{flag_fe_h}=0$, $\text{flag_X_fe} = 0$
- (ii) $-1 < [\text{Fe}/\text{H}] < 0.5$, $-1 < \log g < 6$
- (iii) $3500 < T_{\text{eff}} < 6250$ K, $\text{SNR} = \text{snr_c3_iraf} > 40$
- (iv) $7 < R < 9$, and $|z| < 2$

where $X = \alpha, \text{C}, \text{O}, \text{Mg}, \text{Al}, \text{Si}, \text{Ca}, \text{Mn}, \text{Y}$, and Ba . We set the cut in element abundance to avoid extreme values. The flag_sp , flag_fe_h , and flag_X_fe are set to select stars with reliable stellar parameters and element abundance determination. In addition, we limit the T_{eff} range such that the abundances are not affected by systematic temperature trends. This selection produces agreement between the T_{eff} values from GALAH + DR3 and from angular diameter-based measurements (e.g. Karovicova et al. 2018, 2020) for *Gaia* benchmark stars (Buder et al. 2021). We show in the Appendix in Fig. A1 that there are only small slopes between element abundances $[X/\text{Fe}]$ and T_{eff} . These may be real or systematics inherited from stellar models. We employ a signal-to-noise ratio cut of $\text{SNR} > 40$ for the red band (CCD 3) to ensure good quality spectra, as well as cuts in Galactocentric radius (R) and height from the disc plane (z) to select for disc stars. To ensure a pure sample of stars, we further remove all giants (152 giants in our sample) according to the cut presented in Buder et al. (2021) (i.e. $T_{\text{eff}} < 5500$ K and $\log g < 3.5$ dex). This is because the C abundance of giant stars is affected by internal mixing and dredge-up. This results in a sample of 59 237 stars, and the stellar parameters are shown in Fig. 1. The stars span a range of 0.004–13 Gyrs in age, with a median age = 5.8 Gyrs. The 16th and 84th percentiles of age are 3.7 and 8.6 Gyrs, respectively. Fig. 2 shows the density plots of the parent sample on

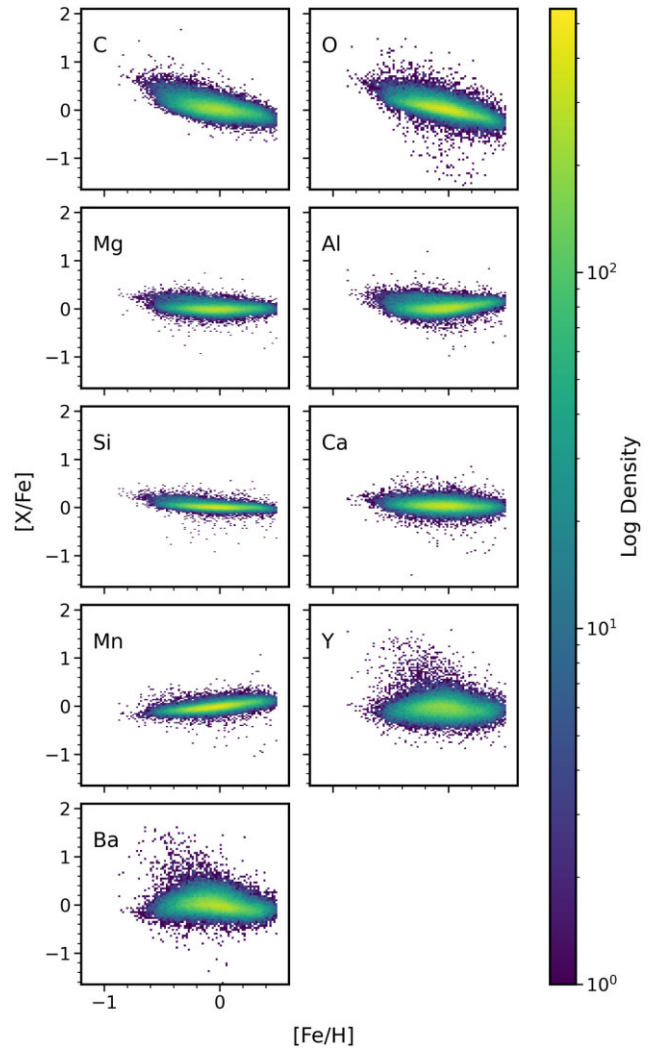


Figure 2. C, O, Mg, Al, Si, Ca, Mn, Y, and Ba abundances of the qualified parent sample of 59 237 stars as a function of metallicity $[\text{Fe}/\text{H}]$, coloured by log density.

$[\text{Fe}/\text{H}]$ – $[X/\text{Fe}]$ plane, for elements C, O, Mg, Al, Si, Ca, Mn, Y, and Ba.

3 METHOD

We aim to determine, given $[\alpha/\text{Fe}]$ and $[\text{Fe}/\text{H}]$ abundances, the distribution of $[X/\text{Fe}]$ across different birth radii (R_{birth}), under an assumed relation between $[\text{Fe}/\text{H}]$ – $[\alpha/\text{Fe}]$ and R_{birth} . Cosmological simulations (e.g. Buck 2020) demonstrate clear birth radius tracks on the $[\text{O}/\text{Fe}]$ versus $[\text{Fe}/\text{H}]$ abundance plane. Fig. 3 is a reproduction of fig. 3 in Buck (2020) for the galaxy g2.79e12, showing the $[\text{O}/\text{Fe}]$ versus $[\text{Fe}/\text{H}]$ plane at solar radius ($7 < R < 9$ kpc). The zoom-in simulation of g2.79e12 analysed in Buck (2020) is taken from NIHAO simulation suite of cosmological hydrodynamical simulations of Milky Way mass galaxies (Wang et al. 2015; Buck et al. 2020). The total virial mass, total stellar mass, and the disc scale length of g2.79e12 are $3.13 \times 10^{12} M_{\odot}$, $15.9 \times 10^{10} M_{\odot}$, and 5.57 kpc. Fig. 3 panels are coloured by (a) birth radius, (b) age, (c) birth radius dispersion, and (d) stellar mass. In Fig. 3(a), stars with high $[\text{O}/\text{Fe}]$ (>0.3) are seen to mostly originate from the inner Galaxy, while stars with low $[\text{O}/\text{Fe}]$ (<0.2) are distributed across a

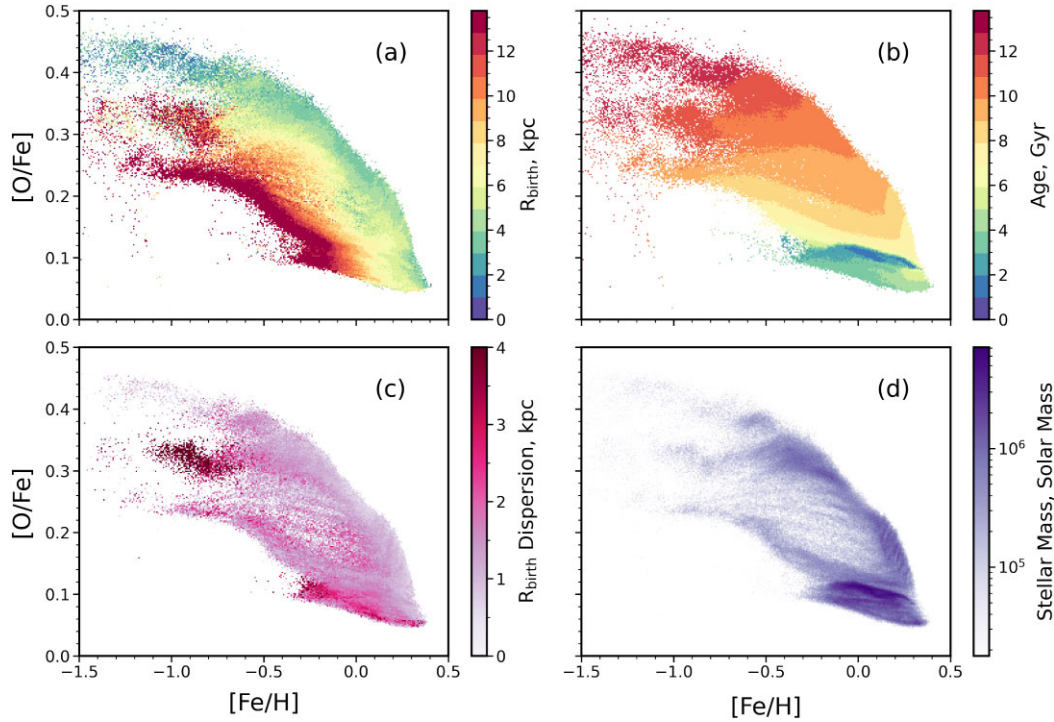


Figure 3. Reproduction of fig. 3 in Buck (2020) for the galaxy g2.79e12, showing the [O/Fe] versus [Fe/H] plane at the solar radius ($7 < R < 9$ kpc) coloured by (a) birth radius, (b) age, (c) birth radius dispersion, and (d) stellar mass.

wider range of birth radii where larger birth radii are offset to lower metallicity. Panel (b) shows clear horizontal age gradients with older ages associated with higher [O/Fe]. In panel (c), there is high birth radius dispersion around $[\text{Fe}/\text{H}] = -1.0$, $[\text{O}/\text{Fe}] = 0.3$, as well as the lower-right region on the [O/Fe] versus [Fe/H] plane towards high metallicity. The stellar mass is also higher in the lower-right region, as shown in panel (d).

Motivated by the results from the Buck (2020) simulations, specifically the birth radius–element abundances trends, we lay down seven R_{birth} tracks (2, 4, 6, 8, 10, 12, and 14 kpc) with equal spacing by eye, as shown in Fig. 4(a) in the $[\alpha/\text{Fe}]$ versus [Fe/H] plane from GALAH data. These tracks qualitatively follow the birth radius gradient on the [O/Fe] versus [Fe/H] plane in Buck (2020) simulation. We then obtained by visual inspection an exponential function that qualitatively best describes the middle track we lay down (i.e. 8 kpc track). The common birth radius range used for Milky Way or Milky Way-like galaxies (e.g. Minchev et al. 2018; Sharma, Hayden & Bland-Hawthorn 2021; Ratcliffe et al. 2023) is around 0–14 kpc. Therefore, we then manually adjust the equation by adding an extra term to the equation that correlates with the birth radius, so that the birth radius tracks that we lay down on the abundance plane cover the range used in other studies. After the adjustment, the equation that describes the R_{birth} tracks becomes

$$R_{\text{birth}} = -40 \times ([\alpha/\text{Fe}] + 0.80 \times \exp(0.4 \times [\text{Fe}/\text{H}] - 0.81)) + 8$$

We further assign every star in our sample a birth radius according to the equation, with known [Fe/H] and $[\alpha/\text{Fe}]$. The number of stars in bins between each track is as follows: 3790 (2–4 kpc), 9298 (4–6 kpc), 15 681 (6–8 kpc), 18 596 (8–10 kpc), 9546 (10–12 kpc), 1304 (12–14 kpc). Stars with assigned $R_{\text{birth}} < 0$ kpc are removed (164 stars, or 0.28 per cent of all qualified disc stars).

Instead of using the oxygen abundance [O/Fe], we choose to use the α -element abundance because (1) it is better measured, as the mean uncertainty in $[\alpha/\text{Fe}]$ is smaller than that of [O/Fe], and (2) in the simulations performed by Buck (2020), [O/Fe] is intended as a tracer of α -elements than of the specific element O. The absolute values of each radial track are not calibrated to match the Milky Way, but the range is consistent with the birth radius range used in other studies, e.g. Frankel et al. 2018. We adopt this form of the relation between [Fe/H]– $[\alpha/\text{Fe}]$ –birth radius and examine the overall effect for the birth radius variations in the element abundance distributions, and for the birth radius at fixed age, if such a relation is held in the Milky Way.

The birth radius increases as $[\alpha/\text{Fe}]$ decreases (from top to bottom), and the y-axis spacing between two neighboring R_{birth} curves is around 0.05 dex. The distribution of the parent sample stars on the $[\alpha/\text{Fe}]$ versus [Fe/H] are also shown in Fig. 4(a) coloured by age, with the median ($[\text{Fe}/\text{H}]$, $[\alpha/\text{Fe}]$) shown as a black circle. We lay down the R_{birth} tracks such that the middle R_{birth} track goes over the median ($[\text{Fe}/\text{H}]$, $[\alpha/\text{Fe}]$) point, adhering to the patterns observed in the simulation (i.e. Buck 2020). As shown in Fig. 3(a), a reproduction of Buck (2020), it is evident that the birth radius of ~ 8 kpc intersects the central portion of the data. Additionally, the distribution of stellar ages exhibits a decreasing trend going towards lower $[\alpha/\text{Fe}]$ and higher [Fe/H] as shown in Fig. 4(a).

As shown in Fig. 4(b), the stellar population density is very non-uniformly distributed in the [Fe/H]– $[\alpha/\text{Fe}]$ plane. We wish to carry out an analysis of how the age and individual abundance distributions of stars change with birth radius, given our R_{birth} model assigned in the [Fe/H]– $[\alpha/\text{Fe}]$ plane. Therefore, the varying density distribution of stars in this plane is not information we wish to propagate. To eliminate the impact of the uneven density of stars in the [Fe/H]– $[\alpha/\text{Fe}]$ plane for this analysis, we use a grid of evenly spaced representative populations in $[\alpha/\text{Fe}]$ versus [Fe/H]. Along the x - and

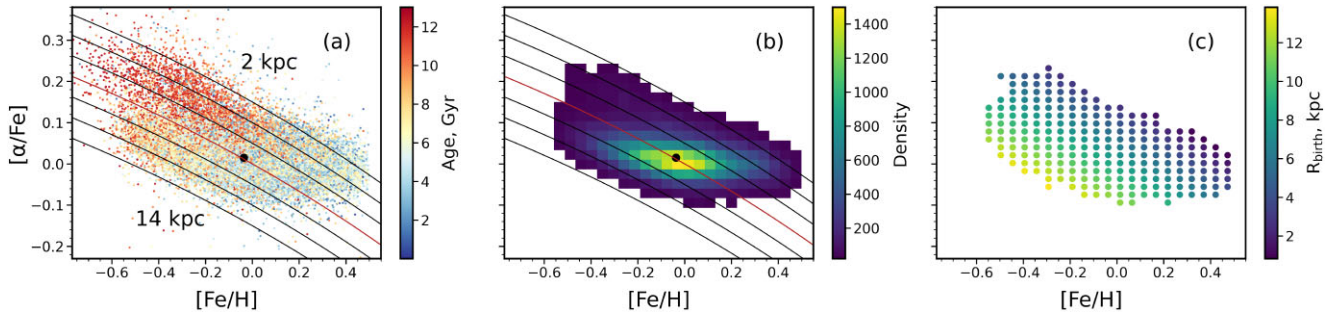


Figure 4. (a) Distribution of the parent sample on the $[\alpha/\text{Fe}]$ versus $[\text{Fe}/\text{H}]$ plane coloured by age. The data covers a region of the stars between $7 < R < 9$ kpc and $|z| < 2$ kpc. The median $[\alpha/\text{Fe}]$ and $[\text{Fe}/\text{H}]$ of the population is indicated by the black point. The curves represent the birth radii assigned to the population. The birth radius increases as going from the top to the bottom curve (top curve: $R_{\text{birth}} = 2$ kpc; bottom curve: $R_{\text{birth}} = 14$ kpc). Specifically, the red curve indicates the median assigned birth radius (8 kpc). (b) Density plot of the parent sample. All bins that have a count less than 20 stars are removed. Birth radius tracks are laid down, and again the median ($[\alpha/\text{Fe}]$, $[\text{Fe}/\text{H}]$) is shown by the black dot. (c) Binned data distribution on $[\alpha/\text{Fe}]$ versus $[\text{Fe}/\text{H}]$ plane, coloured by mean R_{birth} . Stars with assigned $R_{\text{birth}} < 0$ and bins with < 20 stars are removed.

y-axis, the grid spacing is 0.046 and 0.019, respectively. Bins with $N < 20$ stars are removed, mostly on the edges, because we want our binned data to be representative of the neighbouring star population on the abundance plane.

We acknowledge that the density is a major complexity in the Milky Way disc. For example, Sharma, Hayden & Bland-Hawthorn (2021) used an analytical chemodynamic model to explain the distribution of Milky Way stars in the $[\text{Fe}/\text{H}]$ - $[\alpha/\text{Fe}]$ plane based on birth radius and strength of radial migration. As they modelled radial migration, the number density needed to be considered to inform how many stars have moved from their birth place. In contrast, our study examines the analytical relationship observed in simulations for the birth radius, $[\alpha/\text{Fe}]$, and $[\text{Fe}/\text{H}]$ of stars which is not entirely erased by radial migration. Thus, it is not necessary for us to consider the influence of number density on the validity of our proposed analytical relationship.

The remaining sample of 230 binned data points, including 57 730 stars, is summarized in Fig. 4(c) coloured by median birth radius. For each point in panel (c), we calculate a median value for each of the quantities (e.g. age, R_{birth} , and element abundances $[X/\text{Fe}]$) based on the stars within the bin and assign these median values to the binned data point. We use these binned data points along with their assigned values for further analysis. This provides us with an even sampling across the $[\text{Fe}/\text{H}]$ - $[\alpha/\text{Fe}]$ plane in R_{birth} .

4 BIRTH RADIUS DISTRIBUTIONS WITH AGE AND METALLICITY

We explore how the birth radius distribution of stars in the $[\text{Fe}/\text{H}]$ - $[\alpha/\text{Fe}]$ plane as shown in Fig. 4(c) changes as a function of age and metallicity. In Fig. 5, we show the birth radius distribution for a high metallicity ($-0.25 < [\text{Fe}/\text{H}] < 0$, top panel) and low metallicity ($-0.5 < [\text{Fe}/\text{H}] < -0.25$, bottom panel) sample. Within the same metallicity bin, the sample is broken down into three stellar ages bins. These are shown separately with different colours in the sub-panels of Fig. 5, with the lightest to darkest colour for the youngest to oldest stars, respectively. The reason why we focus on $[\text{Fe}/\text{H}] < 0$ when exploring the relationship between age and birth radius is that the age distribution on the $[\alpha/\text{Fe}]$ versus $[\text{Fe}/\text{H}]$ plane is relatively homogeneous in $[\text{Fe}/\text{H}] > 0$ region according to Fig. 4(a), making it less favorable for the study of the age-birth radius relationship.

The mean birth radius values for the three age bins lie at 10.2 kpc (4–6 Gyr bin), 8.2 kpc (6–8 Gyr bin), and 4.9 kpc (8–10 Gyr bin) for

the high metallicity sample, and at 10.7 kpc (6–8 Gyr bin), 8.1 kpc (8–10 Gyr bin), and 5.2 kpc (10–12 Gyr bin) for the low metallicity sample. For both the high and low metallicity samples, the birth radius distribution for older stars generally peaks at a smaller birth radius compared to younger stars, exhibiting an inside–out formation trend similar to other studies (e.g. Minchev et al. 2018; Carrillo et al. 2020; Queiroz et al. 2020). Furthermore, the width of the birth radius distributions also has a correlation with age, in which the width decreases with increasing age. The median absolute deviations (MAD) of the three high metallicity age bins are 1.2 kpc (4–6 Gyr bin), 1.2 kpc (6–8 Gyr bin), and 0.8 kpc (8–10 Gyr bin), and the values for the low metallicity sample are 1.5 kpc (6–8 Gyr bin), 1.2 kpc (8–10 Gyr bin), and 0.8 kpc (10–12 Gyr bin). Here we choose MAD to describe the dispersion because our sample distribution is non-Gaussian, and MAD is less sensitive to extreme values. Under this assumed model between birth radius and the $[\text{Fe}/\text{H}]$ - $[\alpha/\text{Fe}]$ plane, this is consistent with an inside–out formation of the Milky Way; the older stars are more concentrated in the inner Galaxy. The younger stars on the other hand show mean distributions at larger radii and with wider distributions across Galactic radii.

Interestingly, we do not see any obvious age- R_{birth} trends when examining the data across all $[\text{Fe}/\text{H}]$, i.e. without looking at different metallicity bins. This signal is erased, as the mean age distribution is a function of $[\text{Fe}/\text{H}]$, so this age gradient, which is consistent with the idea of ‘inside–out’ formation, is only seen when looking at the distribution of stellar ages in small ranges of $[\text{Fe}/\text{H}]$ in our sample. In the pre-binned data (shown in Fig. 4b), there is a clear density peak in the distribution in the $[\text{Fe}/\text{H}]$ - $[\alpha/\text{Fe}]$ plane; this non-uniform density would presumably enable signatures in age and radius, which are correlated with this plane (i.e. Hayden et al. 2017; Haywood et al. 2019), without metallicity binning, as the majority of stars are at one particular metallicity already. The overall age gradient seen when examining all stars in the Milky Way (e.g. Ness et al. 2016; Hayden et al. 2022) is similarly presumably sensitive to the underlying density distribution of stars as a function of metallicity. This is an example of the Yule–Simpson paradox, a phenomenon in which a trend appears in several groups of data, but disappears or reverses when the groups of data are combined. Examples of Yule–Simpson’s paradox in Galactic archaeology can be found in Minchev et al. (2019). Additionally, samples with different metallicity are dominated by stars of different ages. As shown in Carrillo et al. (2023) Fig. 2, the distribution of current radius R at low metallicity ($[\text{Fe}/\text{H}] = -0.75$) is dominated by 7–10 Gyr old stars, while the

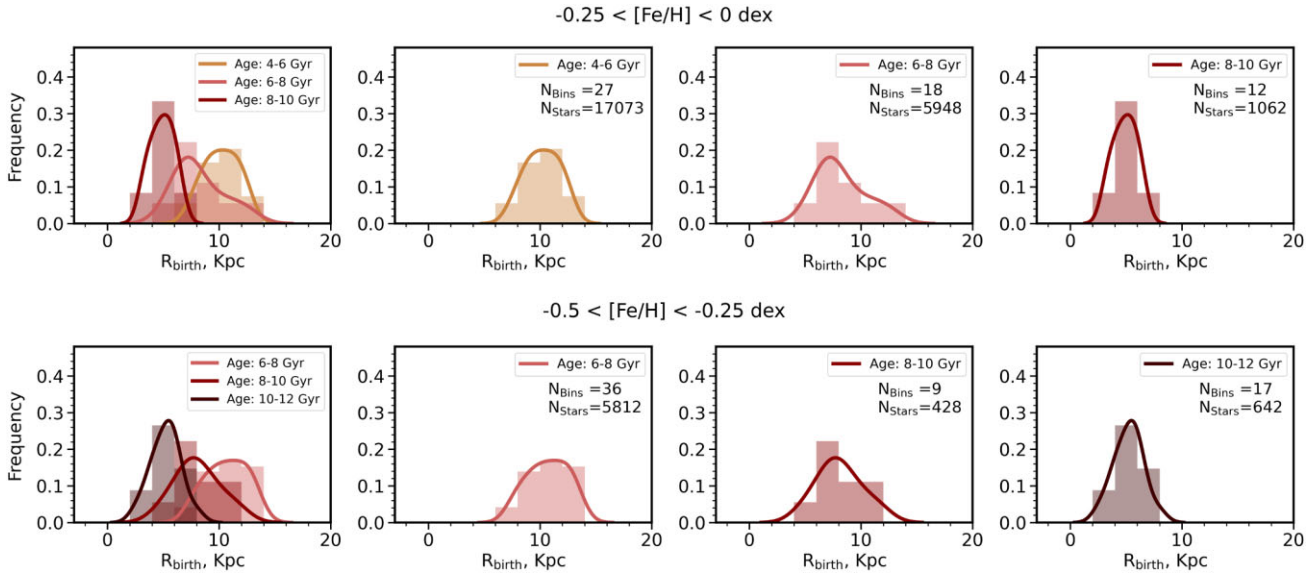


Figure 5. R_{birth} kernel density estimations of high ($-0.25 < [\text{Fe}/\text{H}] < 0$ dex, top panel) and low ($-0.5 < [\text{Fe}/\text{H}] < -0.25$ dex, bottom panel) metallicity stars as sampled from Fig. 4(c). The location of the peaks shows that older stars have a smaller mean birth radius than younger stars, indicating the inside–out formation of the Milky Way. The leftmost sub-panels show the R_{birth} distributions of the three age bins at the same time, whereas the other six sub-panels individually show the R_{birth} distributions of different age bins.

1–3 Gyr old star population becomes the majority at high metallicity ($[\text{Fe}/\text{H}] = 0$). This change in age dominance with $[\text{Fe}/\text{H}]$ also appears in Fig. 5. For the high metallicity sample, we are able to make a bin for 4–6 Gyrs stars but not for 10–12 Gyrs due to having too few old stars in the sample, and this is the opposite in the low metallicity sample. Therefore, we have to make bins according to $[\text{Fe}/\text{H}]$ to account for the differing dominant age populations. In addition, this allows us to see inside–out growth in the level of chemical enrichment for mono-age populations. Comparing the distributions of the two 6–8 Gyr age bins (coloured light pink) in both high and low metallicity samples, we find that the low metallicity sample peaks at a larger R_{birth} . A similar trend also exists in the distributions for age = 8–10 Gyr stars (coloured red). By selecting narrow metallicity bins, we show that the inside–out formation holds for different metallicities.

We summarize the birth radius–age relation, as shown in the top-left panel of Fig. 6. Overall, as the birth radius increases, the stellar age decreases. Similarly, as birth radius increases, the mean metallicity, $[\text{Fe}/\text{H}]$, decreases, as shown in the bottom-left panel of Fig. 6. The top-right panel of Fig. 6 shows the age dispersion as a function of birth radius. We see that small birth radii correspond to the highest age dispersions. Similarly, in the bottom-right panel of Fig. 6, we see that the $[\text{Fe}/\text{H}]$ dispersion is higher at the smaller radii.

5 INDIVIDUAL ABUNDANCE DISTRIBUTIONS AT DIFFERENT BIRTH RADII

We investigate the abundance distributions for the elements C, O, Mg, Al, Si, Ca, Mn, Fe, Y, and Ba, spanning the α , odd- z , iron-peak, and neutron-capture groups of elements, at different birth radii. These $[X/\text{Fe}]$ distributions are shown in Fig. 7. The number of data points from Fig. 4(c) in each of the birth radius bins is 84 (2–6 kpc), 83 (6–10 kpc), and 53 (10–14 kpc).

We find a bimodal distribution towards small birth radius bins. High-precision observational measurements of $[\text{Fe}/\text{H}]-[\alpha/\text{Fe}]$ in the solar neighborhood show a bimodality termed the ‘low’ and ‘high’ α discs (e.g. Bensby, Feltzing & Lundström 2003; Reddy et al.

2003). Across a wider Galactic radius range these change in their density contribution; the high- α sequence is concentrated to the inner Galaxy and the low- α sequence extends to the outer Galaxy (e.g. Hayden et al. 2015). The sampling we use for our analysis is evenly spaced across the full $[\text{Fe}/\text{H}]-[\alpha/\text{Fe}]$ plane as shown in Fig. 4(c). However, when we examine the individual abundance distributions, a bimodality appears in a number of individual elements at the smallest birth radii. This is presumably due to the contribution from both the high- and low- α discs at fixed birth radius in the inner Galaxy. Granted, this is a prediction of our model that the disc is bimodal in elements at small birth radius, but this has been also seen in other works estimating birth radius with a different method (e.g. Ratcliffe et al. 2023). Thus, it is most likely an underlying feature of Milky Way star formation. Furthermore, most of the elements show that the $[X/\text{Fe}]$ distribution changes from wide (2–6 kpc) to narrow (10–14 kpc) as the birth radius increases.

Metallicity, $[\text{Fe}/\text{H}]$: The metallicity distribution at a small birth radius has a higher mean value. A decreasing mean metallicity gradient is observed with present-day guiding radius from the Milky Way centre to the outer region (e.g. Eilers et al. 2022). This is inherited from a birth gradient in the gas metallicity (e.g. Chiappini, Matteucci & Romano 2001; Minchev et al. 2018) but has presumably been weakened by radial migration over time (e.g. Eilers et al. 2022).

Carbon: Carbon is mainly produced in massive stars, followed by low-mass AGB stars (Kobayashi, Karakas & Lugaro 2020). Therefore, carbon distributions should be similar to that of α -elements, as the majority of the α -elements are produced in massive stars. The age-abundance relation for carbon in other observational works (e.g. Bensby & Feltzing 2006; Ness et al. 2019) shows a positive gradient, indicating that $[\text{C}/\text{Fe}]$ is larger for older stars. In this study, the carbon abundance $[\text{C}/\text{Fe}]$ has little relation with R_{birth} value. We see a weak and opposite trend where there is a slight shift in peak position (i.e. larger R_{birth} bins have greater peak $[\text{C}/\text{Fe}]$). However, Carbon changes over the evolution of the star due to dredge-up, so perhaps this is representative of the impact of the intrinsic evolution of the element rather than extrinsic (ISM).

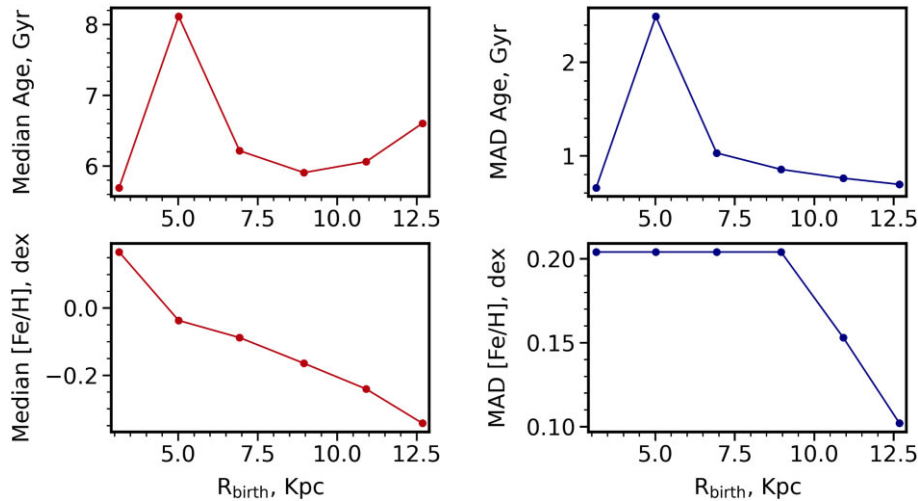


Figure 6. The median and median absolute deviation MAD of age (top row) and metallicity [Fe/H] (bottom row) versus birth radius. Both decrease with increasing R_{birth} .

Oxygen, magnesium, silicon, and calcium (α -elements): For the α -elements Mg, Si, and Ca, the distributions peak at a smaller mean [X/Fe] as the birth radius increases. The α -elements are mainly produced through Type II supernovae and their relative ISM contribution is diluted by the increasing supernovae Ia iron-peak pollution. Therefore, we expect the abundance of α -elements, as a function of iron, to be lower in younger stars. We note that the oxygen abundance [O/Fe] shows the smallest evolution across different birth radii. The distribution is wider at smaller birth radii, and each of the distributions overlaps significantly. We see little variation in [O/Fe] with R_{birth} , which contradicts the progression found in other works (e.g. Delgado Mena et al. 2019; Kobayashi, Karakas & Lugaro 2020).

Manganese (iron-peak): The iron-peak element Mn has a higher mean [Mn/Fe] value toward smaller birth radii. The iron-peak elements like Mn are generally synthesized in Type Ia supernovae and also in collapse supernovae. At the centre of the Milky Way, younger stars are formed from more enriched gas compared to the outskirts of the Galaxy. As [Mn/Fe] increases with [Fe/H] (e.g. Kobayashi, Karakas & Lugaro 2020), [Mn/Fe] is expected to be higher in the Galactic centre compared to that in the outskirts. In the age-abundance trends of Mn examined by Bedell et al. (2018) and Lu et al. (2021), we see that both studies reveal a relatively flat but still positive age-abundance slope. In general, our result agrees with those from the previous studies.

Aluminum (Odd-z): The odd-z element Al also has a higher mean abundance at smaller birth radii. Based on the prediction from the chemical evolution model of the Milky Way, [Al/Fe] decreases with time for stars with age 12 Gyrs and younger (Horta et al. 2021; Fig. 2). Since the majority of our sample stars are younger than 12 Gyrs, we expect our sample to behave similarly (i.e. decreasing [Al/Fe] with time). Moreover, Ness et al. (2019) examined the age-abundance relation of stars at solar metallicity and discovered a positive relation wherein [Al/Fe] increases with increasing age. Such a trend is also seen by Bedell et al. (2018) in their analysis of the Sun-like stars in the solar neighborhood. Thus, [Al/Fe] is expected to increase with decreasing birth radii, as predicted by both the chemical evolution model and the age-[Al/Fe] relation, and as shown in our results.

Barium & yttrium (neutron-capture): The two neutron-capture elements, Ba and Y, though centred on different values, have similar

abundance distributions for stars at different birth radii; that is, the distribution peaks at a larger [X/Fe] value as birth radius increases. They exhibit an opposite trend as the aforementioned elements C, O, Mg, Al, Si, Ca, and Mn. This trend is consistent with the age-abundance relation for the neutron-capture elements from the literature (e.g. Bedell et al. 2018). According to the negative age-[Ba/Fe] relation (Delgado Mena et al. 2019; Horta et al. 2022) as well as the age-birth radius relation (Fig. 6 top-left panel), the older population were born at smaller mean birth radii with a lower [Ba/Fe] value. It is reassuring that Ba and Y have abundance distributions that behave similarly to birth radius, as both are considered s-process elements.

Furthermore, we calculate and tabulate the R_{birth} -[X/Fe] gradients for the low- α stars. In Fig. 8, we present the [X/Fe] versus R_{birth} plots for the low- α in GALAH DR3, with the black lines representing the best-fitting gradients and coloured by log density. The vertical error bar reflects the MAD of [X/Fe] in small R_{birth} bins with bin width = 2 kpc. The gradient results are summarized in Table 1 column 3. The reason we focus on the low- α population is that they exhibit the strongest change in element abundances across radii, but for the high- α stars, there is no obvious abundance trend associated with radius (e.g. Eilers et al. 2022). Adopting Griffith et al. (2022) cuts for low- α stars ([Mg/Fe] > 0.12–0.13[Fe/H] if [Fe/H] < 0; [Mg/Fe] > 0.12 if [Fe/H] > 0), the number of the low- α stars in our sample is $\sim 56\,000$. The inner-most R_{birth} bin (i.e. $R_{\text{birth}} < 5$ kpc) seems to be an outlier to the general trend (referring to Fig. 6). Therefore, to justify a linear fit and gradient metric, we excluded the inner-most R_{birth} data points in our gradient calculations. The gradients are calculated over an R_{birth} range of 5–13 kpc. The largest abundance gradient with R_{birth} is seen in [Fe/H] at -0.066 dex kpc^{-1} followed by the individual element [O/Fe] with an R_{birth} -[X/Fe] slope of 0.028 ± 0.002 dex kpc^{-1} .

We emphasize that in the GALAH sample we use, our present-day radius is limited to the solar neighborhood, with a mean present-day radius of 8.05 ± 0.33 kpc. However, as stars migrate from birth, this survey still gives us access to stars born all over the disc, as parametrized in our model of R_{birth} (from 2–14 kpc). In APOGEE, the survey spans a present-day Galactocentric radius of 0.01–20 kpc, so we can directly compare and contrast our results for birth radius to the present-day radius with APOGEE. For example,

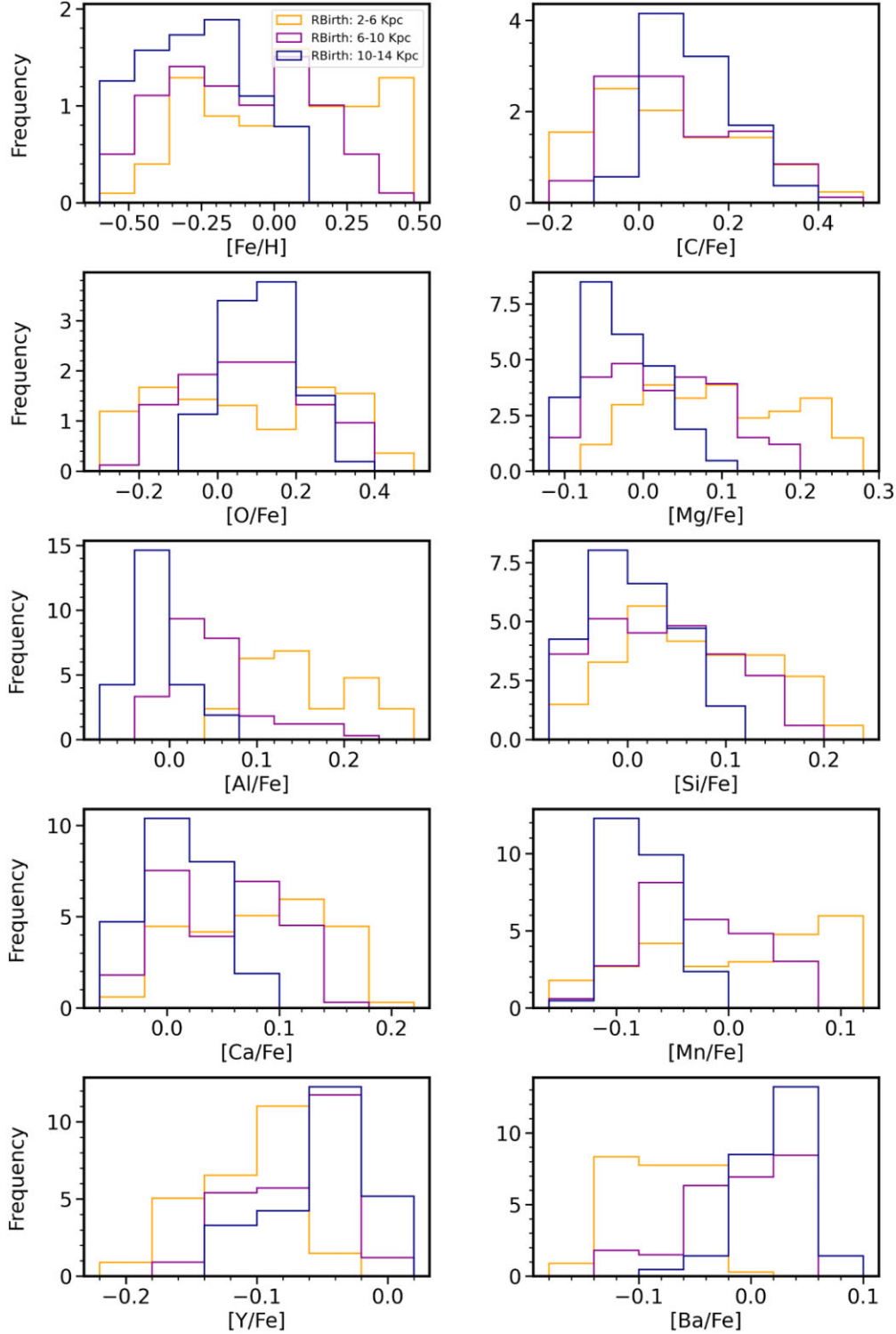


Figure 7. $[X/Fe]$ histogram for data separated in three different birth radius bins, with bin width = 4 kpc. Small R_{birth} bins are coloured in the lightest hue, and large R_{birth} bins are coloured in the darkest hue. In all 10 panels, the elements exhibit distinct distribution trends at different R_{birth} bins, especially in the means and dispersion. Generally, we see that the distributions of smaller R_{birth} bins have larger dispersion, whereas larger R_{birth} bins show smaller dispersion. The median value of each element shows a gradient with R_{birth} .

Table 1 column 1 shows the abundance gradients for APOGEE DR16 low- α disc stars (i.e. $[\alpha/M] < 0.12$, $|z| < 1$) with current radius in the range of 5–13 kpc, obtained from Eilers et al. (2022) fig. 7. We show the seven elements $[X/Fe]$ where $X = \text{C, O, Mg, Al, Si,$

Ca, and Mn) in APOGEE DR17 (Majewski et al. 2017; Abdurro’uf et al. 2022) that are in common with the elements used in this study. We also calculate gradients for the element abundances $[X/Fe]$ independently, using $\sim 63\,000$ APOGEE DR17 low- α stars. We adopt

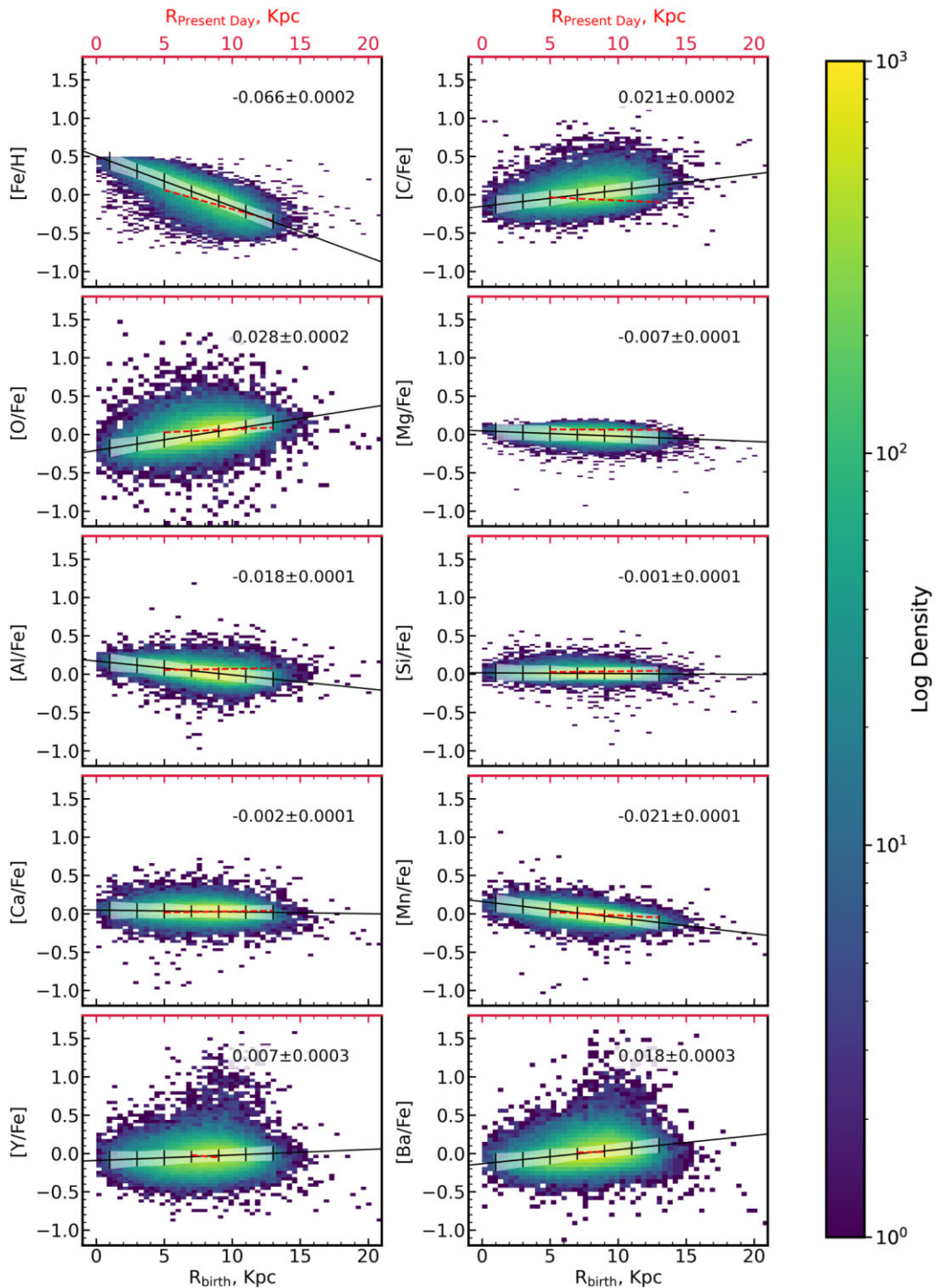


Figure 8. Element abundance $[X/\text{Fe}]$ versus birth radius R_{birth} for GALAH DR3 low- α stars, coloured by log density. The best-fitting $R_{\text{birth}}-[X/\text{Fe}]$ gradient is shown with the black line, and these gradients are summarized in Table 1 column 3. The vertical error bars represent the MAD of $[X/\text{Fe}]$ for stars in different R_{birth} bins, with a bin width of 2 kpc. The red-dashed lines reflect the present-day gradients obtained using APOGEE DR17 (as listed in Table 1 column 2). For Y and Ba which there are no abundance measurements in APOGEE DR17, the red-dashed lines are their GALAH DR3 present-day gradients as shown in column 4.

similar cuts as Eilers et al. (2022) (i.e. $4800 \text{ K} < T_{\text{eff}} < 5800 \text{ K}$, $\log g < 3.6$, $[\alpha/\text{M}] < 0.12$, and $|z| < 1$). The APOGEE gradients are summarized in Table 1 columns 1 and 2. In column 4, since GALAH covers a narrow range in current radius compared to APOGEE, the

present-day radius-abundance gradients for GALAH low- α stars around the solar neighborhood only ($7 < R < 9 \text{ kpc}$) are shown. We discuss these gradient comparisons in more detail in Section 6 below.

Table 1. Current and birth radius $[X/Fe]$ gradients for elements, restricted to low- α stars with $|z| < 1$. Eilers et al. (2022) current radius- $[X/Fe]$ gradients were obtained from their Fig. 7 (from their APOGEE DR16 calibrated abundances).

Element	Eilers et al. (2022) Current (5–13 kpc)	APOGEE DR17 Current (5–13 kpc)	GALAH DR3 Birth (5–13 kpc)	GALAH DR3 Current (7–9 kpc)
Fe	−0.058	−0.050 ± 0.0005	−0.066 ± 0.0002	−0.029 ± 0.003
C	−0.009	−0.008 ± 0.0002	0.021 ± 0.0002	0.000 ± 0.002
O	0.002	0.008 ± 0.0002	0.028 ± 0.0002	0.006 ± 0.002
Mg	0.002	−0.001 ± 0.0002	−0.007 ± 0.0001	0.001 ± 0.001
Al	−0.002	0.003 ± 0.0002	−0.018 ± 0.0001	−0.003 ± 0.001
Si	0.003	0.002 ± 0.0001	−0.001 ± 0.0001	−0.001 ± 0.001
Ca	0.004	0.003 ± 0.0001	−0.002 ± 0.0001	0.002 ± 0.001
Mn	−0.014	−0.009 ± 0.0001	−0.021 ± 0.0001	−0.008 ± 0.001
Y	0.007 ± 0.0003	−0.014 ± 0.002
Ba	0.018 ± 0.0003	0.006 ± 0.002

6 DISCUSSION

In this work, we explore the element abundance distributions of stars as a function of birth radius which we inferred from the $[Fe/H]$ – $[\alpha/Fe]$ plane alone, as motivated by cosmological simulations. We now discuss the validity of our assigned R_{birth} tracks and the implications of our R_{birth} estimates on the star formation history of the Galaxy.

We test two other models for assigning the birth radius. We lay down horizontal and vertical R_{birth} tracks, on the $[\alpha/Fe]$ versus $[Fe/H]$ plane, with smaller R_{birth} assigned to the larger $[\alpha/Fe]$ end in the horizontal assignment and to the larger $[Fe/H]$ end in the vertical assignment. From these alternate R_{birth} tracks, we produce $[X/Fe]$ distributions of these stars with different R_{birth} , similar to Fig. 7. In the horizontal R_{birth} assignment, we see that the mean $[Mn/Fe]$ and $[Fe/H]$ values increase with increasing R_{birth} . This contradicts the observed $[Fe/H]$ gradient (i.e. higher $[Fe/H]$ at the centre) of the Galaxy due to inside–out formation and therefore its longer history of star formation. In addition, there is no obvious trend in the dispersion across different R_{birth} bins for C, O, Al, Mn, Y, and Ba. As for the vertical R_{birth} assignment, the mean abundances of all four α -elements, O, Mg, Si, and Ca, increase with R_{birth} , which does not agree with what is observed with the present-day guiding radius. Observations show that as radius increases the low- α populations dominate and in the inner Galaxy the high- α population has the highest density (e.g. Hayden et al. 2015; Lu et al. 2021). Therefore, the alternative models we propose result in $[X/Fe]$ distributions that are inconsistent with that of observations of present-day guiding radius. However, in general the R_{birth} assignments motivated by the NIHAO-UHD simulations give rise to trends in the individual abundances $[X/Fe]$ that are consistent with observations of element abundance distributions with present-day guiding radius. We have the expectation that the element abundance gradients and dispersions as a function of birth radius will be higher amplitude than that of the present-day guiding radius due to the impact of radial migration. Therefore, this gives us a better insight into the element abundance distributions at stellar birth place and time in the Milky Way disc.

Due to radial migration (e.g. Frankel et al. 2018), we expect gradients in R_{birth} – $[X/Fe]$ to be weakened over time. Therefore, abundance gradients across R_{birth} should be steeper than present-day gradients. This is indeed what we find for most elements.

Using the APOGEE DR16 data, Eilers et al. (2022) reported negative present-day gradients across radii in the low- α disc (i.e. $[\alpha/M] < 0.12$, $|z| < 1$) for $[Fe/H]$, as well as the individual elements $[X/Fe]$ where $X = C, Al, Mn$. For the elements $X = O, Mg, Si, Ca$ they reported positive gradients with Galactic radius. These gradients

are summarized in Table 1 column 1. In column 2 of this table, we report the present-day abundance gradients we calculate with APOGEE. We find good agreement with the Eilers et al. (2022) analysis with the exception of a few elements. We note that the $[Mg/Fe]$ and $[Al/Fe]$ present-day abundance gradients are opposite in sign compared to Eilers et al. (2022) gradients. However, the gradients for these two elements are very shallow. Some differences are not unexpected as we use the APOGEE Stellar Parameter and Chemical Abundances Pipeline (ASPCAP) abundances from APOGEE and Eilers et al. (2022) used a data-driven approach to report calibrated abundances that these gradients are based on. Similarly, we report the present-day gradients in GALAH (column 4) for the low- α stars (adopting Griffith et al. 2022 cuts). Note that the GALAH present-day gradients are over a restricted radius range, compared to APOGEE. Again there are some differences, and the GALAH gradients are shallower than the APOGEE gradients.

The present-day element abundance gradients with radius in columns 1, 2, and 4 of Table 1 serve as a comparison to our calculated birth radius gradients (column 3). We find that the GALAH birth radius gradients are steeper than both the GALAH present-day local gradient (column 4) and APOGEE present-day gradients (with wider present-day radius range; column 1 & 2), except for Y. The magnitude of the change in gradients varies with elements.

For the neutron capture element Y, we find its present-day gradient to be steeper than its birth radius gradient, although opposite in sign. This gradient sign inversion is also seen in other works such as Ratcliffe et al. (2023). In Ratcliffe et al. (2023) fig. 6, they compared the birth and present radius– $[X/Fe]$ gradients of mono-age populations, and this gradient inversion due to radial migration is seen in most radius– $[X/Fe]$ relations they presented, especially in older age bins. Furthermore, if we take the Ce gradient presented in Ratcliffe et al. (2023) as a proxy for Y, as both are neutron-capture elements, we see that (1) there exists the inversion of gradient from older to younger stars, in $[Ce/Fe]$ versus R_{birth} , (2) age tracks do not cleanly separate in the $[Ce/Fe]$ versus R_{birth} plane, and (3) Ce exhibits a non-linear R_{birth} – $[Ce/Fe]$ relationship. All of these might result in the present-day gradient being steeper than the birth radius gradient.

We can therefore infer from our comparisons between columns 1 and 3 that gradients between elements and radius flatten over time. The element $[Fe/H]$ shows the steepest gradient of $-0.066 \text{ dex kpc}^{-1}$ across birth radii. This flattens the order of 12 per cent, to $-0.058 \text{ dex kpc}^{-1}$ from birth to present-day radius, well in agreement with recent theoretical predictions (Buck et al. 2023). The elements $[X/Fe]$ where $X = O, C$, and Mn all have the next steepest gradients from -0.021 to $0.028 \text{ dex kpc}^{-1}$ with birth radius. These flatten by between

$\approx 0.02\text{--}0.03$ dex kpc^{-1} such that the present-day gradients for these elements vary between ≈ -0.014 and 0.002 dex kpc^{-1} . We also note that some of the gradients change sign, between birth and present-day radius (i.e. C, Mg, Si, Ca, and Y). Similar $[X/H]$ radial gradients being flattened over time is also observed in Ratcliffe et al. (2023), in which they used an empirical approach from Lu et al. (2022a) to derive R_{birth} estimates for APOGEE DR17 red giant stars based on their age and $[\text{Fe}/H]$.

The individual abundances of stars as a function of birth radius record the star-forming environment at that location and time in the disc. A recent study by Horta et al. (2022) employed chemical evolution modelling (Rybizki, Just & Rix 2017) to use ages and individual abundances of GALAH stars to infer environmental parameters [i.e. high-mass slope of the Chabrier 2001 IMF (α_{IMF}), number of SN Ia exploding per solar mass over 15 Gyr ($\log_{10}(\text{SNIa})$)]. Their analysis assumed a link between using small bins in $[\text{Fe}/H]$ – $[\text{Mg}/\text{Fe}]$ – $[\text{Ba}/\text{Fe}]$ –age for the chemical evolution model, as representative of linking to the interstellar medium conditions at different birth radii. They subsequently examined the model parameter gradients across present-day radii. They found that the abundances give rise to a gradient in the high-mass end of the disc’s initial mass function. They report that this is more top-heavy towards the inner disc, and more bottom-heavy in the outer disc. Using our birth radius assignment, it would be possible to directly infer the environmental parameters as a function of birth radius and compare the conditions at different birth places and times in the star-forming disc directly.

7 CONCLUSION

This work examines the distribution of individual abundances $[X/\text{Fe}]$ of elements C, O, Mg, Al, Si, Ca, Mn, Y, and Ba for disc stars in different birth radii. To do this, we assumed seven birth radius tracks across the $[\alpha/\text{Fe}]$ versus $[\text{Fe}/H]$ plane of $\sim 59\,000$ GALAH DR3 disc stars and assigned each star a birth radius. This formalism is based on the NIHAO-UHD simulations (Buck 2020) (see Figs 3 and 4). We emphasize that our adopted model of birth radius is not calibrated to quantitatively map a location in the $[\text{Fe}/H]$ – $[\alpha/\text{Fe}]$ plane to the birth radius. Rather, this serves as a tool to trace the element abundance and age distribution of stars across the disc from their origin. Via this approach, we can map variations in time of birth and in individual channels of enrichment to differences in the star-forming environment over time and radius. Below we summarize our main results:

(i) The R_{birth} distribution as a function of age supports an inside-out growth for the Milky Way disc (Fig. 5). There is a larger mean value in R_{birth} for the younger population (i.e. ~ 10 kpc) compared to the older population (i.e. ~ 5 kpc). This result is consistent with a number of earlier studies (e.g. Bensby et al. 2011; Bovy et al. 2012; Minchev et al. 2018).

(ii) The R_{birth} distribution dispersions change with age as well i.e. the median absolute deviation changes from 0.8 to 1.5 kpc going from older to younger stellar populations as the Milky Way disc grows with time and therefore has star formation over a larger region.

(iii) There is a clear progression in the median $[X/\text{Fe}]$ trend with R_{birth} : Mg, Si, Ca, Mn, and Al all decrease while C, O, Y, and Ba all increase with increasing R_{birth} .

(iv) For the low- α population, the abundance gradients are steeper in birth compared to present-day radius. The R_{birth} – $[X/\text{Fe}]$ gradient measures -0.066 ± 0.0002 dex kpc^{-1} compared to the $[\text{Fe}/H]$ present-day gradient of -0.058 dex kpc^{-1} . The $[\text{O}/\text{Fe}]$ abundance is the next strongest indicator of R_{birth} ; it exhibits the steepest R_{birth} – $[X/\text{Fe}]$ slope of the $[X/\text{Fe}]$ measurements (see Table 1) and

is 0.028 ± 0.0002 dex kpc^{-1} in R_{birth} and 0.002 dex kpc^{-1} in present-day.

We tested two other birth radius assignments based on stars’ location on the $[\alpha/\text{Fe}]$ versus $[\text{Fe}/H]$ plane, but neither returned physically plausible $[X/\text{Fe}]$ distributions across radii. Furthermore, our model adopted from the simulation gives sensible results that are aligned with expectations. For example, according to radial migration, we expect birth radius gradients to be steeper in the past, which we find. Therefore, the adopted model for birth radius appears physically plausible and presumably gives insight into the relative distribution of individual abundances across the disc as it formed. Our model uses no direct information about present-day birth radius and is also therefore a useful comparison to models that do assume a relationship with the present-day radius.

In summary, aided by R_{birth} tracks inspired from a cosmological hydrodynamical simulation of a Milky Way-like galaxy and assumptions constrained to the $[\alpha/\text{Fe}]$ versus $[\text{Fe}/H]$ plane, we are able to recover the inside-out growth of the Milky Way disc and the *spatial* evolution in its chemical abundance distributions. This work serves as a proof of concept of the legitimacy of this modelling approach, and in future it can be applied to additional large spectroscopic survey data. This includes data that covers a larger area of the disc, such as the fifth incarnation of the Sloan Digital Sky Survey (SDSS-V) Milky Way Mapper. In addition, chemical evolution modelling would add another dimension in investigating the validity of these R_{birth} assignments (e.g. Buck et al. 2021). Nonetheless, this work shows that assigning birth radius to stars in the Milky Way and studying the element abundance distributions over time and birth place is very promising. This is demonstrative of the utility in using ensembles individual abundances to trace the formation of the Milky Way disc.

ACKNOWLEDGEMENTS

AC acknowledges support from the Science and Technology Facilities Council (STFC) [grant number ST/T000244/1] and the Leverhulme Trust. TB’s contribution to this project was made possible by funding from the Carl Zeiss Stiftung.

DATA AVAILABILITY

The GALAH DR3 data used in this article are available at http://www.galah-survey.org/dr3/the_catalogues. The APOGEE DR17 data used in this article are available at <https://www.sdss4.org/dr17>. Simulation data from the NIHAO-UHD project is available at https://tobias-buck.de/#sim_data. Other data used in this article can be made available upon reasonable request to the corresponding authors.

REFERENCES

- Abdurro’uf et al., 2022, *ApJS*, 259, 35
 Adibekyan V. Z., Sousa S. G., Santos N. C., Delgado Mena E., González Hernández J. I., Israelian G., Mayor M., Khachatryan G., 2012, *A&A*, 545, A32
 Bahcall J. N., Loeb A., 1990, *ApJ*, 360, 267
 Bedell M. et al., 2018, *ApJ*, 865, 68
 Bensby T., Feltzing S., 2006, *MNRAS*, 367, 1181
 Bensby T., Feltzing S., Lundström I., 2003, *A&A*, 410, 527
 Bensby T., Alves-Brito A., Oey M. S., Yong D., Meléndez J., 2011, *ApJ*, 735, L46
 Bovy J., 2015, *ApJS*, 216, 29
 Bovy J., Rix H.-W., Liu C., Hogg D. W., Beers T. C., Lee Y. S., 2012, *ApJ*, 753, 148

- Buck T., 2020, *MNRAS*, 491, 5435
- Buck T., Obreja A., Macciò A. V., Minchev I., Dutton A. A., Ostriker J. P., 2020, *MNRAS*, 491, 3461
- Buck T., Rybizki J., Buder S., Obreja A., Macciò A. V., Pfrommer C., Steinmetz M., Ness M., 2021, *MNRAS*, 508, 3365
- Buck T., Obreja A., Ratcliffe B., Lu Y. L., Minchev I., Macciò A. V., 2023, *MNRAS*, 523, 1565
- Buder S. et al., 2021, *MNRAS*, 506, 150
- Carrillo A., Jøgee S., Drory N., Kaplan K. F., Blanc G., Weinzirl T., Song M., Luo R., 2020, *MNRAS*, 493, 4094
- Carrillo A., Ness M. K., Hawkins K., Sanderson R. E., Wang K., Wetzel A., Bellardini M. A., 2023, *ApJ*, 942, 35
- Chabrier G., 2001, *ApJ*, 554, 1274
- Chiappini C., Matteucci F., Romano D., 2001, *ApJ*, 554, 1044
- Clarke A. J. et al., 2019, *MNRAS*, 484, 3476
- Cui X.-Q. et al., 2012, *Res. Astron. Astrophys.*, 12, 1197
- de Mijolla D., Ness M. K., Viti S., Wheeler A. J., 2021, *ApJ*, 913, 12
- De Silva G. M. et al., 2015, *MNRAS*, 449, 2604
- Delgado Mena E. et al., 2019, *A&A*, 624, A78
- Dotter A., Conroy C., Cargile P., Asplund M., 2017, *ApJ*, 840, 99
- Eilers A.-C., Hogg D. W., Rix H.-W., Ness M. K., Price-Whelan A. M., Mészáros S., Nitschelm C., 2022, *ApJ*, 928, 23
- Frankel N., Rix H.-W., Ting Y.-S., Ness M., Hogg D. W., 2018, *ApJ*, 865, 96
- Frankel N., Sanders J., Rix H.-W., Ting Y.-S., Ness M., 2019, *ApJ*, 884, 99
- Freeman K., Bland-Hawthorn J., 2002, *ARA&A*, 40, 487
- Gilmore G. et al., 2012, *The Messenger*, 147, 25
- González Delgado R. M. et al., 2015, *A&A*, 581, A103
- Griffith E. et al., 2021, *ApJ*, 909, 77
- Griffith E. J., Weinberg D. H., Buder S., Johnson J. A., Johnson J. W., Vincenzo F., 2022, *ApJ*, 931, 23
- Hayden M. R. et al., 2015, *ApJ*, 808, 132
- Hayden M. R., Recio-Blanco A., de Laverny P., Mikolaitis S., Worley C. C., 2017, *A&A*, 608, L1
- Hayden M. R. et al., 2022, *MNRAS*, 517, 5325
- Haywood M., Snaith O., Lehnert M. D., Di Matteo P., Khoperskov S., 2019, *A&A*, 625, A105
- Horta D. et al., 2021, *MNRAS*, 500, 1385
- Horta D., Ness M. K., Rybizki J., Schiavon R. P., Buder S., 2022, *MNRAS*, 513, 5477
- Iben Icko J., 1965, *ApJ*, 142, 1447
- Karovicova I. et al., 2018, *MNRAS*, 475, L81
- Karovicova I., White T. R., Nordlander T., Casagrande L., Ireland M., Huber D., Jofré P., 2020, *A&A*, 640, A25
- Kobayashi C., Karakas A. I., Lugaro M., 2020, *ApJ*, 900, 179
- Kos J. et al., 2018, *MNRAS*, 473, 4612
- Lu Y. L., Angus R., Curtis J. L., David T. J., Kiman R., 2021, *AJ*, 161, 189
- Lu Y., Minchev I., Buck T., Khoperskov S., Steinmetz M., Libeskind N., Cescutti G., Freeman K. C., 2022a, preprint ([arXiv:2212.04515](https://arxiv.org/abs/2212.04515))
- Lu Y., Buck T., Minchev I., Ness M. K., 2022b, *MNRAS*, 515, L34
- Majewski S. R. et al., 2017, *AJ*, 154, 94
- McMillan P. J., 2017, *MNRAS*, 465, 76
- Minchev I., Quillen A. C., 2006, *MNRAS*, 368, 623
- Minchev I., Famaey B., Quillen A. C., Di Matteo P., Combes F., Vlahjić M., Erwin P., Bland-Hawthorn J., 2012, *A&A*, 548, A126
- Minchev I. et al., 2018, *MNRAS*, 481, 1645
- Minchev I. et al., 2019, *MNRAS*, 487, 3946
- Ness M., Hogg D. W., Rix H. W., Martig M., Pinsonneault M. H., Ho A. Y. Q., 2016, *ApJ*, 823, 114
- Ness M. K., Johnston K. V., Blancato K., Rix H. W., Beane A., Bird J. C., Hawkins K., 2019, *ApJ*, 883, 177
- Ness M. K., Wheeler A. J., McKinnon K., Horta D., Casey A. R., Cunningham E. C., Price-Whelan A. M., 2022, *ApJ*, 926, 144
- Piskunov N., Valenti J. A., 2017, *A&A*, 597, A16
- Queiroz A. B. A. et al., 2020, *A&A*, 638, A76
- Quillen A. C., Minchev I., Bland-Hawthorn J., Haywood M., 2009, *MNRAS*, 397, 1599
- Ratcliffe B. L., Ness M. K., 2023, *ApJ*, 943, 92
- Ratcliffe B. et al., 2023, *MNRAS*, 525, 2208
- Recio-Blanco A. et al., 2023, *A&A*, 674, A29
- Reddy B. E., Tomkin J., Lambert D. L., Allende Prieto C., 2003, *MNRAS*, 340, 304
- Rybizki J., Just A., Rix H.-W., 2017, *A&A*, 605, A59
- Sellwood J. A., Binney J. J., 2002, *MNRAS*, 336, 785
- Sharma S. et al., 2018, *MNRAS*, 473, 2004
- Sharma S., Hayden M. R., Bland-Hawthorn J., 2021, *MNRAS*, 507, 5882
- Shetrone M. et al., 2019, *ApJ*, 872, 137
- Ting Y.-S., Conroy C., Goodman A., 2015, *ApJ*, 807, 104
- Valenti J. A., Piskunov N., 1996, *A&AS*, 118, 595
- Wang L., Dutton A. A., Stinson G. S., Macciò A. V., Penzo C., Kang X., Keller B. W., Wadsley J., 2015, *MNRAS*, 454, 83
- Weinberg D. H. et al., 2022, *ApJS*, 260, 32
- Zhao G., Zhao Y.-H., Chu Y.-Q., Jing Y.-P., Deng L.-C., 2012, *Res. Astron. Astrophys.*, 12, 723

APPENDIX: ELEMENT ABUNDANCE VERSUS EFFECTIVE TEMPERATURE

We include here the element abundance $[X/Fe]$ versus effective temperature T_{eff} plot in Fig. A1. There exist small temperature– $[X/Fe]$ gradients as quantified in the figure. To test whether or not the temperature gradients affect our $R_{\text{birth}}-[X/Fe]$ results, we redid our $R_{\text{birth}}-[X/Fe]$ gradient calculations with temperature restricted to a very narrow range of $5300 \text{ K} < T_{\text{eff}} < 5600 \text{ K}$ – where these temperature gradients are relatively flat – and find that the results are consistent with what we find using the broader range.

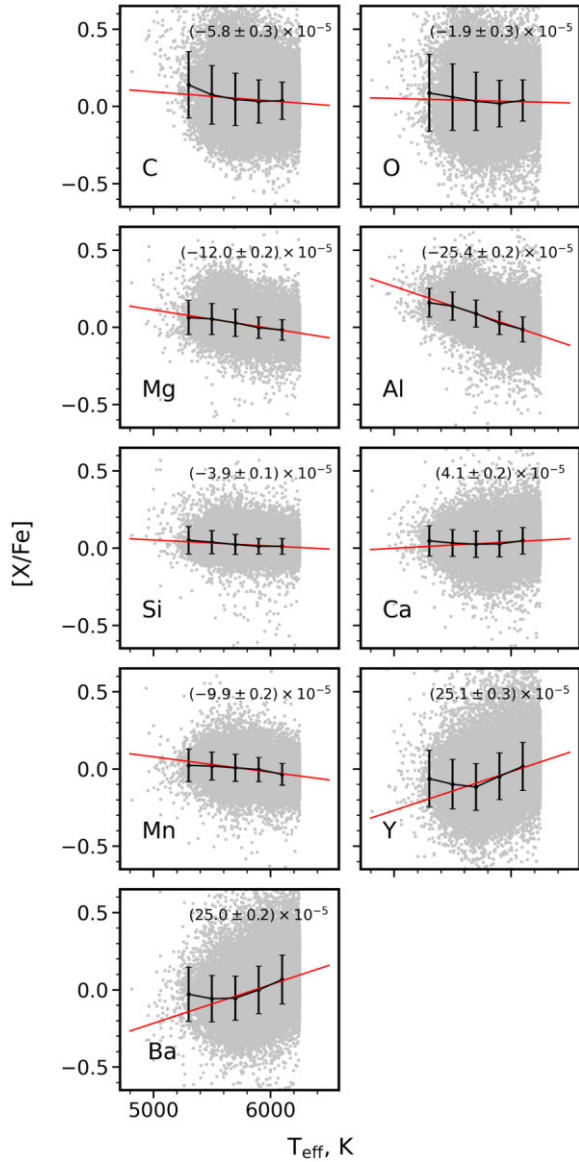


Figure A1. Element abundance $[X/Fe]$ versus effective temperature T_{eff} . The mean and scatter is shown in black solid dots as a function of T_{eff} . The $T_{\text{eff}}-[X/Fe]$ gradients are presented in the panels, obtained from fitting the scattered data. The red lines are the best fit.

This paper has been typeset from a $\text{\TeX}/\text{\LaTeX}$ file prepared by the author.